

# Studies and Theoretical Optimization of CL-20:RDX Cocrystal

Jalla Venkata Viswanath,<sup>[a, b]</sup> Balaiah Shanigaram,<sup>[c]</sup> Panga Vijayadarshan,<sup>[a, b]</sup> T. Venkaiah Chowadary,<sup>[b]</sup> Amarnath Gupta,<sup>[b]</sup> Kotamarthi Bhanuprakash,<sup>[c]</sup> Siddapura Ramachandrappa Niranjana,<sup>[a]</sup> and Abbaraju Venkataraman<sup>\*[a, d]</sup>

**Abstract:** CL-20 among other nitramines is highly energetic along with the high positive heat of formation, and is a green energetic material employed as solid propellant [1–3]. However, it suffers basically from mechanical sensitivity and cost of synthesis. Cocrystallization of CL-20 with other suitable HEMs and LEMs is considered as the best crystal engineering technique to reduce its sensitivity [2,4–6] as it masks crystal defects which in turn are responsible for mechanical sensitivity. The present investigation reports on the scale up process for the synthesis of Energy-Energy Cocrystallization (EECC) of  $\epsilon$ -CL-20 and RDX and focus on the process to optimize the structure and energetics of thus formed cocrystal (CRCC) through DFT study. In our study CL-20 and RDX are taken in 1:1 molar ratio as sug-

gested by Gui-yun Hang [7]. We claim successful scale up of cocrystallization to the earlier report [4] employing a more user friendly solvent (acetone) in the present study and the cocrystal formed was through ultra centrifugation. During the course of the cocrystal formation a phase transition from  $\epsilon$ - to  $\alpha$  took place. The Trauzl lead block tests on CRCC support the better performance of the synthesised EECC. Introducing shock tube test as the parameter to claim the strength of HEMs enhances the comparability [8]. The present report envisages and collaborates the synthesised CRCC through the theoretical study in arriving at the spatial conformation leading to optimization in structure and energy of the synthesized EECC.

**Keywords:** Low sensitive High Energy Material (LSHEM) • Cocrystallization • Secondary bonding • Theoretical structure optimization • Gaussian

## 1 Introduction

Tailoring physical and chemical properties with the aid of secondary bonds without altering the intrinsic structure of the molecule is the basic principle of cocrystallization technique [6]. The crystal densities and crystal defects can be avoided employing this crystal engineering technique involving two or more sub crystals. The risk of adulteration with external materials is low, as the technique involves only physical bonding and the obtained cocrystals are structurally homogenous. The secondary bonding studies in cocrystal involves O–H, O–O and O–N of two sub crystals. The possibility of formation of secondary bonds can be predicted from the morphology of the molecule and the atomic orientations. Cocrystallization is studied widely in pharmaceutical sector, where the active pharmaceutical ingredient (API) is crystal engineered with conformers (sub crystals) so as to make it commercially marketable [9]. The problems of solubility, dissolution rate, bioavailability, physical stability, flowability, chemical stability, compressibility and hygroscopicity are successfully dealt by cocrystallizing an API with suitable coformers. This principle is applied in the field of High Energy Materials (HEMs) to synthesize a new HEM with improved characteristics [9–10]. Obtaining Low sensitive High Energy Material (LSHEMs) out of conven-

tional HEMs is the challenge to date, as they involve controlling the factors that are responsible for their high sensitivity without affecting the sub crystal's energetics.

The CL-20 is a nitramine as shown in Figure 1 has a cage structure. The cage structure is attributed from the C1–C4 bond which joins the top of two five member rings (FMRs) contains alternative carbon and nitrogen atoms, while the bottom portion form a boat shape 6 member ring (SMRs) in its skeleton. The cage structure thus formed has the strain

- [a] J. V. Viswanath, P. Vijayadarshan, S. R. Niranjana, A. Venkataraman  
Materials Chemistry Laboratory, Department of Materials Science, Gulbarga University  
Kalaburagi-585106, Karnataka, India  
\*e-mail: raman.dms@gmail.com
- [b] J. V. Viswanath, P. Vijayadarshan, T. V. Chowadary, A. Gupta  
R&D centre, Premier Explosives Limited  
Peddakandukur-508286, Telangana, India
- [c] B. Shanigaram, K. Bhanuprakash  
Catalysis and Fine Chemicals Department, CSIR-Indian Institute of Chemical Technology  
Hyderabad 500007, India
- [d] A. Venkataraman  
Department of Chemistry, Gulbarga University  
Kalaburagi-585106, Karnataka, India

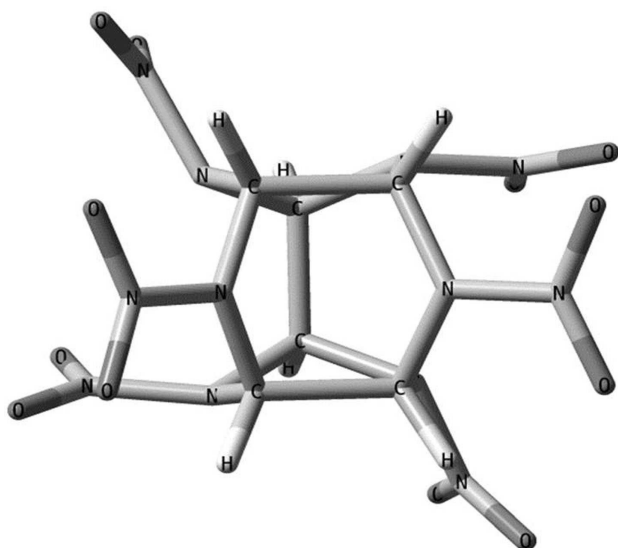


Figure 1. Tube form of CL-20 molecule

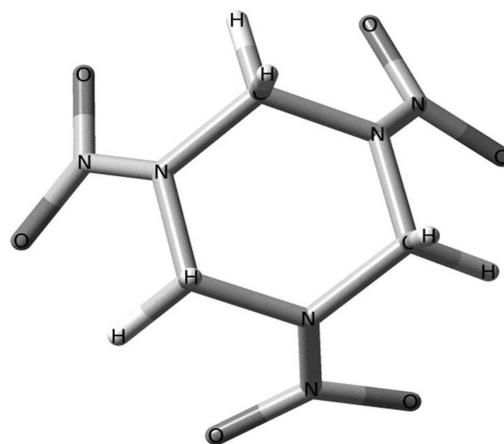


Figure 2. Tube form of RDX molecule

in the structure and is called the Conventional Ring Strain Energy (CRSE) [2]. The CRSE of CL-20 makes it special and more energetic out of other cyclic nitroamines viz. RDX and HMX. CRSE of CL-20 gives the skeleton an additional positive energy ( $\Delta H_f = +454.0 \text{ kJ} \cdot \text{mol}^{-1}$ ) and high density ( $\sim 2040.0 \text{ kg} \cdot \text{m}^{-3}$ ). Despite of high CRSE, crystal of CL-20 clouded with defects (voids) which restrict its wide commercial applicability [2]. Chaoyang Zhang et al. [11] and Nilgun Sen [12] have claimed the shear sliding of crystal layers caused due to mechanical stress influences mechanical sensitivity of explosives. Crystal voids in CL-20 are one of the hotspots which are responsible for mechanical sensitivity [13–14]. It is understood that an increase in inter/intramolecular potentials of sub crystals at shear slide would make them less sensitive to the mechanical stimuli. The inter/intramolecular potentials of sub crystals are understood to be enhanced by secondary bond formation between sub crystals during cocrystallization thus becoming mechanically less sensitive [12]. In cocrystallization technique the crystal voids of CL-20 are understood to be masked through the formation of secondary bonds between the sub crystals, thus reducing the risk of shear sliding of layers and thereby reducing the mechanical sensitivity in the material [15]. RDX is also a nitramine with six-member ring having alternate carbon and nitrogen atoms in the skeleton shown in Figure 2. The structurally optimized RDX has one nitro group in axial and two nitro groups in equatorial positions [16]. The possible secondary bonds are understood to be formed between O atom (Donor) of RDX nitro group and the H-atom (Acceptor) of  $\epsilon$ -CL-20. The formation and study of this EECC is understood to help the industry in many fronts e.g., a strategic material with greater internal energy, structural stability, affordability (RDX synthesis is economical on comparison with CL-20), mechanical insensitivity and required shock

tube detonation velocity. Hence it was found interesting to understand the structure, bonding and theoretical energies associated with the structure, and the same is presented in this report.

Shock tube is a tool employed to carry the shock wave uninterrupted to blast detonators. Shock tube is used mostly in underwater and mine detonations where detonating fuse may not work. The polymer tube has an inner lining of uniformly spread HEM (mostly PETN) with uniform particle size ( $\approx 100 \mu\text{m}$ ). The shock wave created at one end of the shock tube is carried forward to the destination uninterrupted due to uniform HEM spreading [8]. The detonation velocity of shock tube plays an important role in determining the safety parameters of the blast. However our intention is to determine how fast the shock wave propagates with our CRCC.

We have employed the Trauzl lead block test to demonstrate the increased strength of newly formed CRCC. The enlargement of hole on the lead block may reveal the intensity of blast caused due to respective HEM. Higher the enlargement of hole it is considered as higher the HEM strength.

Among most of the existing cocrystals of CL-20,  $\beta$  and  $\gamma$ -forms were used.  $\epsilon$ -form has large lattice energy and compact crystal packing among other polymorphs, which makes it unfavourable to form cocrystal with other sub crystals [15]. Earlier reports on synthesis and theoretical studies of cocrystals include sub crystals between  $\beta$  or  $\gamma$  forms of CL-20 and other low sensitive HEMs (viz. HMX, TNT and BTF) and with non energetic viz. polymeric material (Caprolactam) [17]. In all the reports, the authors explained their observations based on the secondary bonds, particularly hydrogen bonds with a designed crystal orientation and spatial arrangement.

Some reports in the literature on the synthesis of HEM cocrystals include the following: Adam Matzger and Onas Bolton have synthesised CL-20/TNT and CL-20/HMX cocrystals by complete solvent evaporation and dehydration of

the individually mixed HEM slurry. The characterized cocrystals are mixed with other group D explosives and employed as potential detonators [18]. In the selected sub crystals, one of them is highly sensitive compared to the other viz. CL-20 is highly sensitive when compared with HMX, TNT and BTF. Changyan Guo et al. used a non high energetic organic compound namely caprolactam to reduce the sensitivity of CL-20. The authors stated strong intermolecular hydrogen bonds formation between CL-20 and caprolactam sub crystals responsible for the formation of cocrystals [17]. Chaoyang Zhang et al. studied the CL-20/HMX, CL-20/TNT and CL-20/BTF cocrystal using various theoretical methods, which include hydrogen bond formation [15], Hirshfeld surface determination, Radial distribution functions and interaction energies. The authors proposed that the  $\omega$ B97X-D function with basis set superposition errors (BSSE) is the promising theoretical calculation where the cocrystals formed are thermodynamically controlled. The reduced band gap in cocrystals to that of its respective sub crystals inferred the reported cocrystals are energetically favoured [15]. Zongwei Yang et al. reported the synthesis of CL-20/BTF EECC. The EECC formed has reduced detonation pressure and velocity of detonation to that of BTF and possessed the better detonation properties [6]. In recent report, Mirnal Ghosh et al. reported the synthesis of EECC with CL-20 and HMX having stoichiometric mixture 2:1 through solvent evaporation in presence of high boiling anti solvent and the authors observed better thermokinetic parameters with improved velocity of detonation and reduced sensitivity than CL-20 [19]. Zongwei Yang et al. reported that the CL-20 cocrystal with TNT using N-methyl Pyrrolidone (NMP) as solvent and observed the reduced sensitivity of CL-20 with a predicted detonation performance similar to that of trinitrotoluene (TNT) and 2,4-dinitroanisole (DNAN) [20]. Xianfeng Wei et al. reported the BTF based cocrystals and the PIXEL calculations used to calculate energies of cocrystals. The authors have used M06-2X/6-311 + G (d,p) of Gaussian 09 to calculate potential energy density of hydrogen bonds of the synthesized cocrystals [21]. Xianfeng Wei et al. reported 12 different EECCs that are thermodynamically favoured which include CL-20/TNT, CL-20/BTF and CL-20/HMX etc. [5]. The authors also studies theoretical investigation including COMPASS, PIXEL, B3LYP, and  $\omega$ B97X-D functions to predict the lattice energies and thermodynamic parameters viz. changes in internal energy, entropy and Gibbs free energy. The authors have predicted the formation of EECC to be thermodynamically favoured, and also obtained that dominance of entropy as a sufficient parameter to that of enthalpy is predicted in the formation of cocrystal with the choice of proper solvent [5]. A recent review by S. Zeman et al. gives the clear predictions of HEMs, formation of their cocrystals and the strategies from formation including the mechanical behaviour thus obtained though the strategy adapted [22]. A clear understanding on the sensitivity and performance of energetic materials has been explained in the review. The authors have explained

the relationship between sensitivity and performance based on several fractions and particularly on heat of formation [22].

Spray flash technique, ultrasonic spray assisted-electrostatic adsorption and bead mill aqueous suspension techniques are employed to synthesise CL-20/HMX nano cocrystals and the authors have reported the mean particle size of less than 200 nm [23–25]. Chongwei An et al. recently reported spray flash synthesis of nano  $\epsilon$ -CL-20/HMX cocrystal with reduced impact and friction sensitivity than CL-20 [26]. Haifeng Xu et al. reported CL-20/TATB cocrystals by rapid nucleation of solvent and non-solvent technique and achieved a low sensitive energetic-energetic cocrystal (LSECC) [27]. From the above studies, the inference may be drawn that cocrystals obtained employing  $\epsilon$ -CL-20 through special techniques will circumvent the difficulty and facilitate the formation of EECC.

Present work is an attempt to cocrystallize  $\epsilon$ -CL-20 with RDX while retaining its energetics. The ultra sonication assisted slow solvent evaporation technique facilitates the formation of EECC and this is also further supported by the theoretical investigations shown in the latter part. CRCC is characterized with PXRD, FTIR, SEM and TGA/DTA to understand crystal structure, molecular structure, morphology and thermal behaviour respectively. Density function theory (DFT) is used to model and optimize the structure and energetics of the synthesised CRCC. Though Han Gao et al. [4] have reported the synthesis of CL-20 and RDX cocrystal, an approach for scale up and theoretical optimization supports its applicability further. Change in the solvent employed in the earlier report [4] embraces the solvent effect on cocrystallization and CL-20 phase transition.

## 2 Experimental

### 2.1 Materials and Methods

The HEMs (CL-20 and RDX) are supplied in anhydrate form with 99% purity by Premier Explosives Limited, Hyderabad, India. Facility for cocrystallization, Trauzl lead block test and shock tube detonation velocity of CRCC and the sub crystals are provided by Premier Explosives Limited, Hyderabad, India. Enthalpy standard procedures as reported wherever necessary, while the computational studies and the calculations are done at CSIR-IICT, Hyderabad, India.

### 2.2 Cocrystallization

4.38 g CL-20 and 2.22 g RDX (1:1 molar ratio) are added to 45 ml of analytical grade acetone (because of its high solubility) and stirred well to dissolve and the solution is then kept overnight for homogeneity. This solution is subjected to ultrasound assisted evaporation between 43–45 °C (i.e. below the boiling point of solvent) for a period of 3 hours.

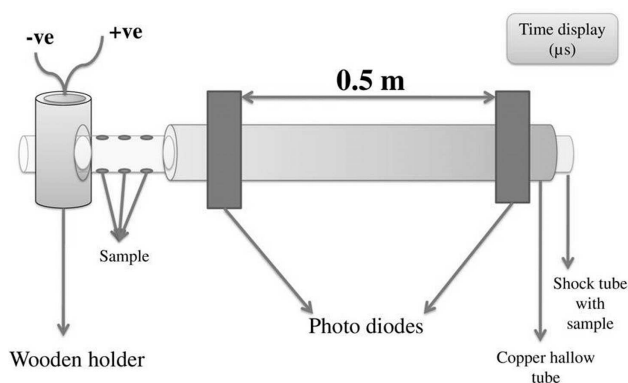


**Figure 3.** Shock tube detonation velocity testing apparatus

The obtained colourless crystals are washed with water and vacuum dried before testing for its melting point, density and was subjected to further characterization and studies.

## 2.3 Characterization Techniques

Crystal structure of synthesized CRCC is determined using Philips XRD made Philips instrument and the result is compared with the JCPDS files individually to that of  $\epsilon$ -CL-20 and  $\alpha$ -CL-20 and RDX. Functional groups, molecular interactions and the formation of hydrogen bonds in the cocrystal is elucidated employing Bruker FTIR instrument (JASCO IR-5300 spectrometer) at the resolution of  $4\text{ cm}^{-1}$  with 256 scans. Scanning Electron Microscope (HITACHI SU-1500) is employed to determine the crystal morphology of the cocrystal. Thermal behaviour (TGA and DTA) of the cocrystal is studied from room temperature to  $300^\circ\text{C}$  using SHIMADZU, DTG-60H instrument under a dynamic flow of nitrogen with a flow rate of  $20\text{ ml/min}$  and heating rate of  $10^\circ\text{C/min}$ .

## 2.4 Performance Tests

### 2.4.1 Trauzl Lead Block Test

A Trauzl lead block test is employed as per the standard procedure [28] to understand the performance of a HEM. The procedure adopted here involves a lead block of  $\sim 9.5\text{ kg}$  weight and  $101.5 \pm 0.5\text{ mm}$  diameter. This block is drilled to have a cavity of  $54.5 \pm 0.5\text{ mm}$  length and  $7.1 \pm 0.25\text{ mm}$  diameter. The cavity is filled with a detonator containing Aluminium shell with  $45\text{ mm}$  length and  $6.85\text{ mm}$  diameter,  $250.5 \pm 0.5\text{ mm}$  of primary explosive (NHN) which is procured from premier Explosives Limited, Hyderabad, India,  $23\text{ mg}$  of normal fuse head with a small plug and a test sample viz., CL-20, RDX and CRCC of  $300 \pm 0.5\text{ mg}$  each separately for each experiment. The detonator is blasted using fuse head wire and the expansion in the cavity is measured

using water. Aluminium contamination is cleared before measuring the volume.

### 2.4.2 Shock Tube Detonation Velocity

Shock tube is a tool to carry shock wave from one end to another without getting objected or disturbing the environment in the vicinity. The HEM used to line the inner core of shock tube must possess the qualities to carry the shock wave smooth and fast. Though flowability, particle size and density play major roles in choosing best HEM for shock tube, the performance of HEM to carry shock wave uninterrupted and fast are to be kept as important aspect. The principle of investigating detonation velocity measurement is based on the ability of the photodiode sensors to receive a light signal when the detonation wave arrives and to transmit that signal to suitable measuring equipment. The setup adopted is according to the standard procedure [28].

The procedure involves a copper tube of approximately  $60\text{ cm}$  on which two photodiodes are placed at a distance of  $50\text{ cm}$ . Shock tube containing sample lining is fitted into the copper tube. One end of shock tube is inserted into a wooden holder where it is connected to an external electric initiator. The photodiodes are connected to a microsecond watch so as to measure the time. The electric initiator fires the sample which is lined in the shock tube. A shock wave travels through the length of the shock tube. Starting photodiodes detect the shock wave starting time and ending photodiode detects the ending time. As the distance between photodiodes is  $50\text{ cm}$ , the time taken for the shock wave to travel the distance between two diodes is measured employing micro timer. With these inputs, we have calculated the detonation velocity using equation 1, given below. The set up of shock tube velocity of detonation equipment is shown in Figure 3.

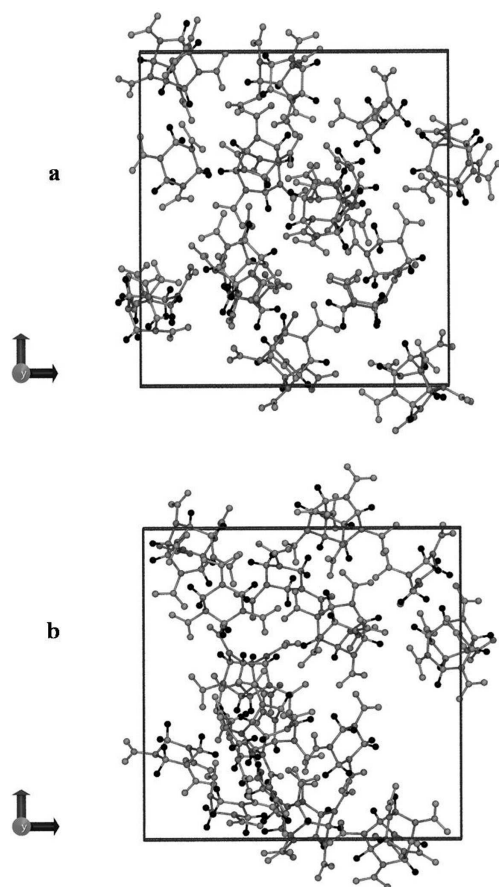
$$\text{Detonation velocity} = d/t \quad (1)$$

$d$  = distance between photo diodes ( $0.5\text{ m}$ )

$t$  = time taken for the light to travel between photo diodes ( $\mu\text{s}$ ).

## 3 Computational Studies

Molecular Dynamics (MD) simulations followed by Density Functional Theory (DFT) calculations were carried out to understand the cocrystal formation between RDX and CL-20 molecules. Individual crystal structures of RDX and CL-20 were taken as an initial guess for optimization of the individual molecules. Based on an earlier study, among different packing molecular ratios of RDX and CL-20, 1:1 molecular ratio is found to be the most stable one [7]. Hence 1:1 ratio is considered in this study.

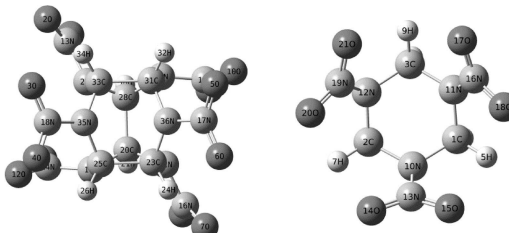


**Figure 4.** a) Packing of CL-20 and RDX in a cubic box of 21 Å length before 200ps NVT simulations, b) Packing of CL-20 and RDX in a cubic box of 21 Å length after 200ps NVT simulations

To get various conformations of the cocrystals, MD simulations were performed using LAMMPS package [29] and, a generalized amber force field GAFF [30] in NVT ensemble is used to describe interactions between all atoms. Periodic boundary conditions (PBC) were applied in all directions. The temperature was kept constant at 300 K by Nose-Hoover thermostat. Initial individual topology input for LAMMPS was generated with the help of Moltemplate package [31]. 8 individual molecules each of RDX and CL-20 (1:1 ratio) were packed into a cubic box of size 21 Å as shown in Figure 4. The partial charges on each atom of the molecules are assigned using RESP method and are given in Table 1 [32–33].

First energy minimization, followed by an NVT simulation for 200 ps with 1 fs time step was performed. Long-range electrostatic interactions were calculated with particle-particle-particle mesh solver (PPPM) [34]. LJ (Lennard-Jones) cut-off distance of 10 Å is considered in the simulations. From the simulated structure of cocrystal packing shown in Figure 4(b), various conformers were selected as shown in the Figure 5. Such 13 conformers from MD simulations were further fully optimized using DFT at dispersion

**Table 1.** Partial charges for CL-20 and RDX from RESP Method.

					
S.No.	ATOM	Charge	ATOMS	Charge	
1	O	−0.350489	C	0.145245	
2	O	−0.351246	C	0.151172	
3	O	−0.376233	C	0.155381	
4	O	−0.363005	H	0.120087	
5	O	−0.363893	H	0.148241	
6	O	−0.377141	H	0.118569	
7	O	−0.351521	H	0.146332	
8	O	−0.350414	H	0.117716	
9	O	−0.363071	H	0.144764	
10	O	−0.335803	N	−0.438871	
11	O	−0.362728	N	−0.439471	
12	O	−0.335223	N	−0.442160	
13	N<O	0.603649	N<	0.859748	
14	N<O	0.605881	O	−0.417710	
15	N<O	0.607603	O	−0.418048	
16	N<O	0.603819	N<	0.858949	
17	N<O	0.676626	O	−0.417538	
18	N<O	0.673621	O	−0.417525	
19	N	−0.120870	N<	0.862516	
20	C	−0.117318	O	−0.418652	
21	H	0.244773	O	−0.418746	
22	N	0.011310			
23	C	0.024716			
24	H	0.214160			
25	C	−0.099441			
26	H	0.224317			
27	N	0.011629			
28	C	−0.116877			
29	H	0.245144			
30	N	−0.124572			
31	C	−0.090657			
32	H	0.222496			
33	C	0.022395			
34	H	0.213382			
35	N	−0.124942			
36	N	−0.130078			

corrected functional  $\omega$ B97X-D [35] and meta-hybrid functional M06-2X [36–37] employing a 6-31G(d, p) basis set using the Berny optimization algorithm with a default convergence criteria and integration grid implemented in Gaussian 09 software package [38]. Frequency calculations were performed at the same level of theory to ensure that the optimized geometries are the true local minima on the potential energy surface with zero imaginary frequencies. No symmetry constraints were applied during geometry relaxation.

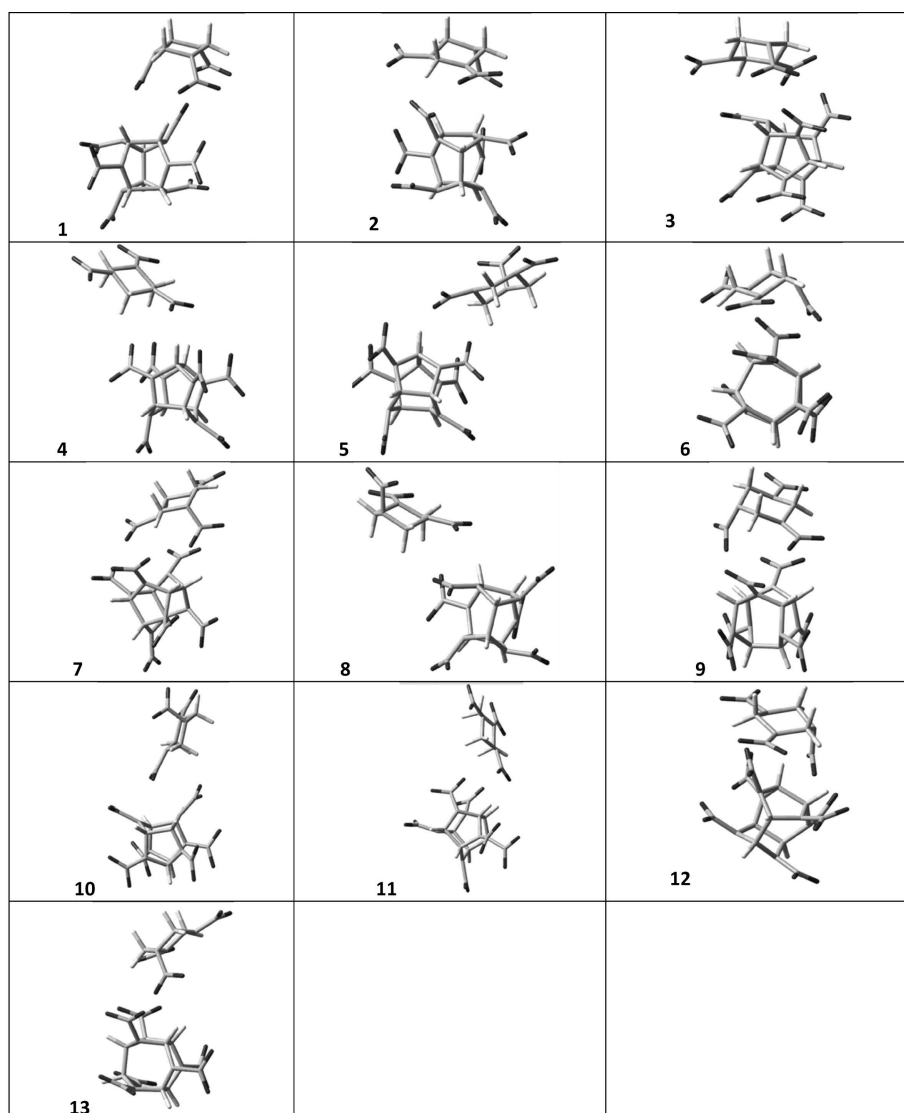


**Figure 5.** Different conformers of RDX and CL-20

Binding energies (BE) for the conformers were calculated to predict the most stable conformers of the cocrystal as the energy difference between the isolated molecules and cocrystal as shown in the equation 2.

$$\Delta E = E_{\text{RDX-CL-20}} - (E_{\text{CL-20}} + E_{\text{RDX}}) \quad (2)$$

where,  $\Delta E$  is the binding energy between CL-20 and RDX.

$E_{\text{CL-20}}$  is the energy of isolated CL-20

$E_{\text{RDX}}$  is the energy of isolated RDX

$E_{\text{RDX-CL-20}}$  is the energy of CL-20 and RDX cocrystal

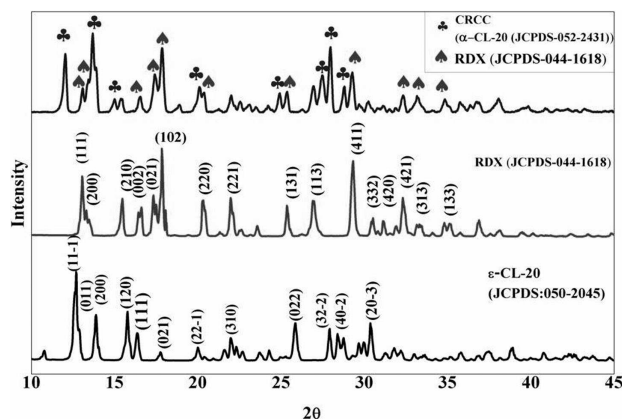
Here, for binding energy calculations, M06-2X and ωB97X-D functionals were considered because these functionals have been found to perform well in molecules with weak intermolecular interactions [35–36, 39].

Thermal analysis was carried out on the frequency calculations. Thermodynamic properties like entropy, enthalpy and free energy for all the conformers are analysed which give an idea about the feasibility of formation of RDX-CL-20 cocrystal and its thermal stability.

## 4 Results and Discussion

The dried CRCC powder shows the melting point in the range of 180 °C to 200 °C (MP of ε-CL-20 and RDX are 171 °C and 204 °C respectively) and is characterized to understand its crystal structure, molecular bonds (primary and secondary) and crystal morphology employing PXRD, FTIR and SEM techniques respectively. The interpretations are given below.



PXRD patterns of  $\epsilon$ -CL-20, RDX and CRCC**Figure 6.** Comparison between PXRD patterns of  $\epsilon$ -CL-20, RDX and CRCC

PXRD patterns of pure sub crystals ( $\epsilon$ -CL-20 and RDX) and CRCC are shown in Figure 6. The PXRD peaks of  $\epsilon$ -CL-20 and RDX sub crystals matches with the JCPDS file no.050-2045 and JCPDS file no.044-1618 respectively and are shown in Table 2. The PXRD pattern of CRCC has characteristic peaks of  $\alpha$ -CL-20 (JCPDS-052-2431) with small shifts. They are viz., at a  $2\theta$  angle of  $12.04^\circ$ ,  $13.68^\circ$ ,  $15^\circ$ ,  $20.1^\circ$  and  $27.96^\circ$  [40]. The peaks at  $2\theta$  of  $13.08^\circ$ ,  $13.44^\circ$ ,  $16.54^\circ$ ,  $17.4^\circ$ ,  $17.84^\circ$ ,  $20.38^\circ$ ,  $22^\circ$ ,  $25.36^\circ$ , and  $29.28^\circ$  in Figure 6 are the characteristic PXRD peaks of RDX [41]. A variation in the PXRD pattern peak intensities represents crystal

**Table 2.** PXRD peaks of pure sub crystals (CL-20 and RDX) and CRCC.

$\epsilon$ -CL-20 (JCPDS:050-2045)		RDX (JCPDS:044-1618)		CRCC
$2\theta$	(hkl)	$2\theta$	(hkl)	$2\theta$
12.57	(111)	13.04	(111)	12.04 a
12.75	(011)	13.30	(200)	13.08 b
13.82	(200)	15.46	(210)	13.44 b
15.77	(120)	16.42	(002)	13.68 a
16.32	(111)	17.33	(021)	15 a
17.75	(021)	17.49	(211)	16.54 b
19.98	(221)	17.82	(102)	17.4 b
21.96	(310)	20.32	(220)	17.84 b
25.83	(022)	21.96	(221)	20.1 a
27.91	(322)	23.56	(122)	20.38 b
28.38	(402)	25.34	(131)	22 b
30.3	(203)	26.90	(113)	24.92 a
		29.32	(411)	25.36 b
		30.51	(332)	27.46 a
		31.14	(420)	27.96 a
		32.31	(421)	28.8 a
		33.29	(313)	29.28 b
		34.80	(241)	
		35.09	(133)	
		36.88	(233)	

a)  $\alpha$ -CL-20 (JCPDS file no.052-2431). b) RDX (JCPDS:044-1618).

phases of CRCC. The negligible  $\Delta 2\theta$  to that of pure sub crystals represents almost no crystal strain in CRCC. Crystal planes corresponding to  $2\theta$  of  $30.42^\circ$  and  $31.14^\circ$  of RDX [41] are missing in the PXRD pattern of CRCC, this behaviour may be due to the involvement of the particular crystal faces in the interaction between the two sub-crystals.

The FTIR spectrum of CRCC is shown in Figure 7a. Broad band between  $1622.13\text{ cm}^{-1}$  to  $1531.47\text{ cm}^{-1}$  and  $1352\text{ cm}^{-1}$  to  $1219\text{ cm}^{-1}$  in the FTIR spectrum of CRCC represents the mixing of  $\text{NO}_2$  asymmetric stretching peaks of  $\epsilon$ -CL-20 ( $1607\text{ cm}^{-1}$ ,  $1590\text{ cm}^{-1}$  and  $1568\text{ cm}^{-1}$ ), RDX ( $1535\text{ cm}^{-1}$ ,  $1576$  and  $1593\text{ cm}^{-1}$ ) and  $\text{NO}_2$  symmetric vibration peaks of  $\epsilon$ -CL-20 ( $1352\text{ cm}^{-1}$  to  $1266\text{ cm}^{-1}$ ), RDX ( $1267\text{ cm}^{-1}$  and  $1275\text{ cm}^{-1}$ ) respectively. Stacking of nitro groups in CRCC may be the reason behind broadening of the above-said peaks. The characteristic peaks corresponding to a  $\text{CH}_2$  skeleton of RDX ( $1388.74\text{ cm}^{-1}$ ,  $1423.46\text{ cm}^{-1}$ ,  $1433.11\text{ cm}^{-1}$  and  $1458.18\text{ cm}^{-1}$ ) are retained in the cocrystal depicting disentanglement of RDX's  $\text{CH}_2$  skeleton in secondary bonding. C–H symmetric stretching peaks of  $\epsilon$ -CL-20 ( $3045\text{--}3016\text{ cm}^{-1}$ ) are shifted and forms pentet of peaks with  $\text{CH}_2$  asymmetric stretching peaks of RDX at  $3022\text{ cm}^{-1}$ ,  $3035\text{ cm}^{-1}$ ,  $3051\text{ cm}^{-1}$ ,  $3064\text{ cm}^{-1}$  and  $3074\text{ cm}^{-1}$ .  $\text{CH}_2$  symmetric stretching peaks of RDX are appeared at  $2947\text{ cm}^{-1}$  and  $3001\text{ cm}^{-1}$  for CRCC. The FTIR spectrum of CRCC shows a triplet peak at  $745\text{ cm}^{-1}$  ( $730\text{ cm}^{-1}$ ,  $750\text{ cm}^{-1}$  and  $763\text{ cm}^{-1}$ ) and a doublet at  $823\text{ cm}^{-1}$  and  $835\text{ cm}^{-1}$  which are signature peaks of  $\alpha$ -CL-20 [42]. The FTIR peaks of pure CL-20 taken for the synthesis of CRCC however clearly matches with the  $\epsilon$ -CL-20 [43] and is shown in the Figure 7b. Hence it is understood from the FTIR that the  $\epsilon$ -CL-20 sub-crystal changed to  $\alpha$ -CL-20 during CRCC formation.  $\alpha$ -CL-20 in the cocrystal is also reported by Haifeng Xu et al. [27]. Shift in C–H symmetric stretching peaks ( $\Delta$ ) of  $\epsilon$ -CL-20 from  $3013\text{ cm}^{-1}$  to  $3022\text{ cm}^{-1}$  and  $3043\text{ cm}^{-1}$  to  $3051\text{ cm}^{-1}$  along with  $\Delta$  in  $\text{NO}_2$  symmetric stretching of RDX from  $1266\text{ cm}^{-1}$  to  $1219\text{ cm}^{-1}$  are expected to be due to the formation of secondary bonds i.e., Hydrogen bonding between 'H' in CH group in  $\epsilon$ -CL-20 and 'O' in  $\text{NO}_2$  of RDX. The comparison of FTIR peaks of individual sub crystals and CRCC is given in Table 3.

SEM image of  $\epsilon$ -CL-20 shown in Figure 8a has predominantly rhombohedral crystals of different sizes. The irregular RDX particles shown in Figure 8b are confirmed based on the earlier literature [44]. Figure 8c and 8d clearly show the sharpness of CL-20 crystal edges being masked and distortion in the orthorhombic structure is also observed. This behaviour may be due to the formation of secondary bonds between  $\epsilon$ -CL-20 and RDX which also leads to reduced sensitivity [2].

TG analysis of  $\epsilon$ -CL-20 as shown in Figure 9 has a first weight loss of 2.03% from room temperature to  $236.2^\circ\text{C}$  and RDX has a weight loss of 17.78% from room temperature to  $230.3^\circ\text{C}$  whereas the CRCC shows a weight loss of 4.54% up to  $213.4^\circ\text{C}$  from room temperature. A sudden weight loss of 87.23% at  $215^\circ\text{C}$  from the first weight loss

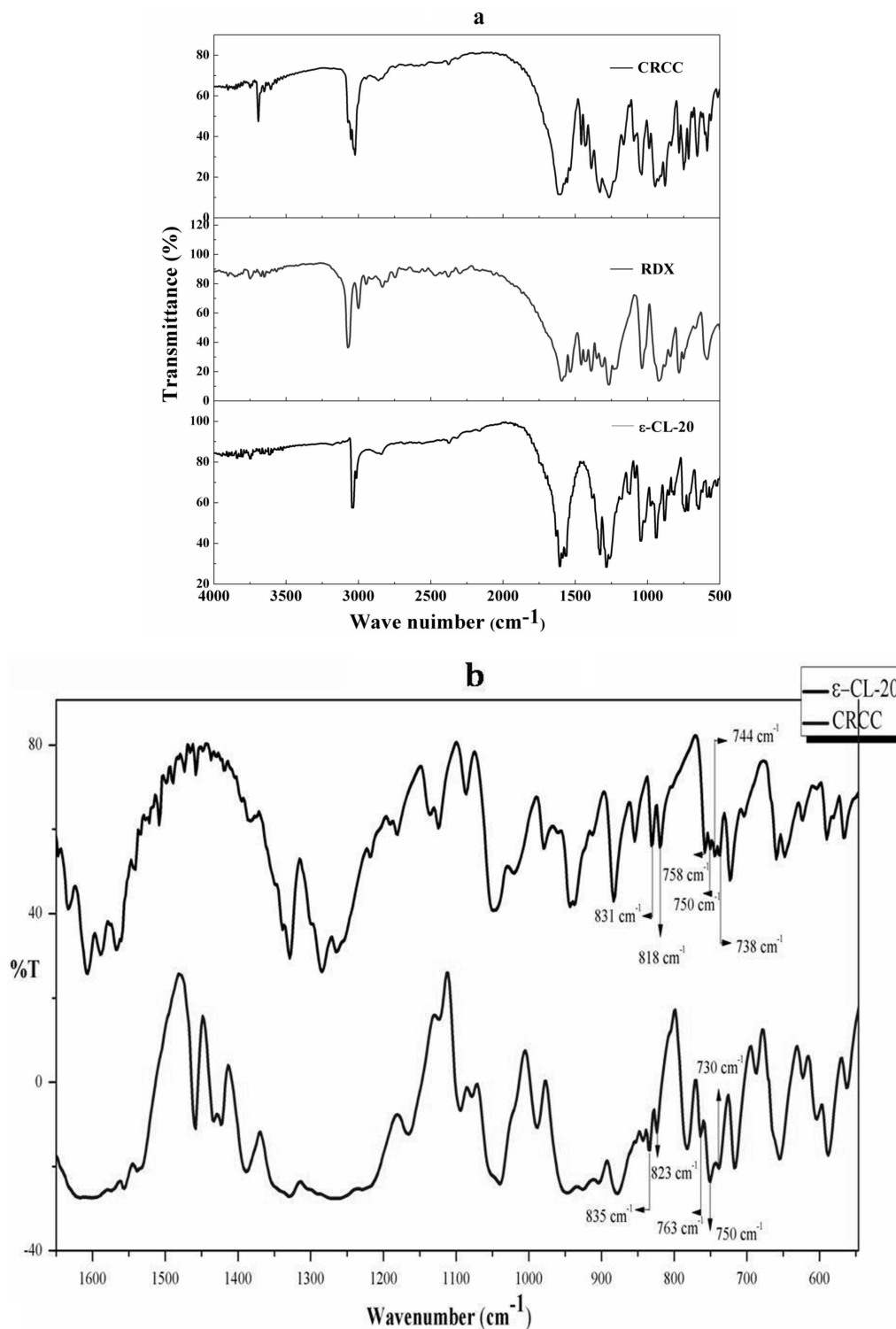


**Figure 7.** a) Comparison between FTIR spectra of  $\epsilon$ -CL-20, RDX and CRCC, b) Signature peaks comparison of  $\epsilon$ -CL-20 and CRCC

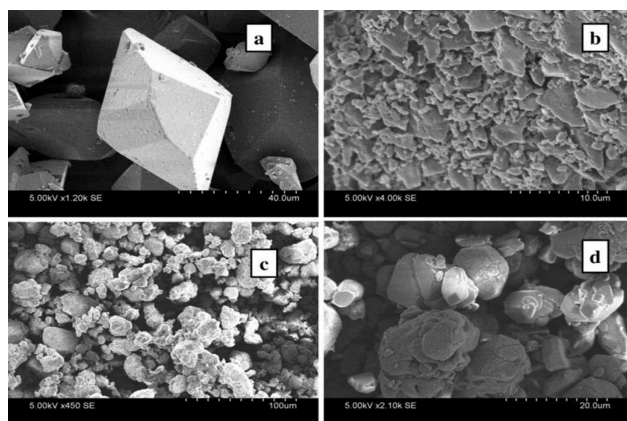
for CRCC is noticed and it differs from either of the sub crystals (95.27% for  $\epsilon$ -CL-20 at 239°C and 79.22% for RDX at 230.5°C from respective first weight losses). TGA graphs of sub crystals and CRCC are shown in Figure 9. Sudden

weight loss from 213.4°C to 215°C in the TGA of CRCC confirms the feature of cocystal instead of physical mixture [27]. DTA curve of cocystal shown in Figure 10 has a single exothermic peak along with several endothermic peaks. The



Table 3. comparison between FTIR peaks of CRCC,  $\epsilon$ -CL-20 and RDX.

$\epsilon$ -CL-20 Peak	Assignment	RDX Peak	Assignment	CRCC Peak	Assignment
3045 $\text{cm}^{-1}$ and 3016 $\text{cm}^{-1}$	—CH symmetric stretching	3074 $\text{cm}^{-1}$ and 3064 $\text{cm}^{-1}$	—CH <sub>2</sub> asymmetric stretching	3074 $\text{cm}^{-1}$ , 3064 $\text{cm}^{-1}$ , 3051 $\text{cm}^{-1}$ , 3035 $\text{cm}^{-1}$ and 3022 $\text{cm}^{-1}$	—CH symmetric stretching of CL-20 and —CH <sub>2</sub> asymmetric stretching of RDX
1633 $\text{cm}^{-1}$ , 1606 $\text{cm}^{-1}$ , 1589 $\text{cm}^{-1}$ and 1568 $\text{cm}^{-1}$	—NO <sub>2</sub> asymmetric stretching	1593 $\text{cm}^{-1}$ , 1576 $\text{cm}^{-1}$ and 1535 $\text{cm}^{-1}$	—NO <sub>2</sub> asymmetric stretching	1622.13 $\text{cm}^{-1}$ to 1531.47 $\text{cm}^{-1}$	—NO <sub>2</sub> asymmetric stretching
1384 $\text{cm}^{-1}$ w, 1348 $\text{cm}^{-1}$ vw, 1338 $\text{cm}^{-1}$ , 1328 $\text{cm}^{-1}$ , 1284 $\text{cm}^{-1}$ , 1265 $\text{cm}^{-1}$ and 1219 $\text{cm}^{-1}$	—CH bend, —NO <sub>2</sub> symmetric vibration band	1458 $\text{cm}^{-1}$ , 1433 $\text{cm}^{-1}$ , 1423 $\text{cm}^{-1}$ and 1388 $\text{cm}^{-1}$	CH <sub>2</sub> skeleton	1383 $\text{cm}^{-1}$ , 1458 $\text{cm}^{-1}$ , 1433 $\text{cm}^{-1}$ , 1423 $\text{cm}^{-1}$ and 1394 $\text{cm}^{-1}$	O—H bending (hydroxyl) CH <sub>2</sub> skeleton
1180 $\text{cm}^{-1}$ , 1136 $\text{cm}^{-1}$ and 1124 $\text{cm}^{-1}$	—CH bend	1275 $\text{cm}^{-1}$ and 1267 $\text{cm}^{-1}$	—NO <sub>2</sub> symmetric vibration band	1352 $\text{cm}^{-1}$ to 1219 $\text{cm}^{-1}$	—CH bend, NO <sub>2</sub> symmetric vibration band
1085 $\text{cm}^{-1}$	Ring stretch	1232 $\text{cm}^{-1}$ and 1217 $\text{cm}^{-1}$	C—H bend	1165 $\text{cm}^{-1}$ , 1122 $\text{cm}^{-1}$ , 1095 $\text{cm}^{-1}$	—CH bend Ring stretch Ring stretch, N—N stretch
1049 $\text{cm}^{-1}$	Ring stretch, N—N stretch	1039 $\text{cm}^{-1}$	Ring stretch	1053 $\text{cm}^{-1}$ to 1039 $\text{cm}^{-1}$	Ring stretch, N—N stretch of CL-20 and RDX
1020 $\text{cm}^{-1}$	Ring stretch, N—N stretch	1018 $\text{cm}^{-1}$	Ring stretch		
980 $\text{cm}^{-1}$ , 943 $\text{cm}^{-1}$ , 937 $\text{cm}^{-1}$ , 912 $\text{cm}^{-1}$ , 883 $\text{cm}^{-1}$ , 854 $\text{cm}^{-1}$	Ring deformation	945 $\text{cm}^{-1}$ , 923 $\text{cm}^{-1}$ , 914 $\text{cm}^{-1}$ , 881 $\text{cm}^{-1}$ , 852 $\text{cm}^{-1}$ , 842 $\text{cm}^{-1}$	Symmetric ring stretch	989 $\text{cm}^{-1}$ , 950 $\text{cm}^{-1}$ to 902 $\text{cm}^{-1}$ , 877, 852 $\text{cm}^{-1}$	Ring deformation Symmetric ring stretch
819 $\text{cm}^{-1}$ and 831 $\text{cm}^{-1}$	C—C stretching			823 $\text{cm}^{-1}$ and 835 $\text{cm}^{-1}$	C—C stretching
758 $\text{cm}^{-1}$ , 750 $\text{cm}^{-1}$ , 744 $\text{cm}^{-1}$ , 738 $\text{cm}^{-1}$	—NO <sub>2</sub> deformation	781 $\text{cm}^{-1}$ , 752 $\text{cm}^{-1}$ , 736 $\text{cm}^{-1}$	—NO <sub>2</sub> deformation	781 $\text{cm}^{-1}$ , 763 $\text{cm}^{-1}$ , 750 $\text{cm}^{-1}$ , 738 $\text{cm}^{-1}$ , 717 $\text{cm}^{-1}$	—NO <sub>2</sub> deformation
723 $\text{cm}^{-1}$	—NO bend; N—NO <sub>2</sub> bend				—NO bend; N—NO <sub>2</sub> bend
660 $\text{cm}^{-1}$ , 648 $\text{cm}^{-1}$	—NO bend			686 $\text{cm}^{-1}$	—NO bend



SEM image of CRCC at (a)  $\epsilon$ -CL-20, (b) RDX, (c) CRCC 100  $\mu\text{m}$ , (d) CRCC 20  $\mu\text{m}$

Figure 8. SEM image of CRCC at (a)  $\epsilon$ -CL-20, (b) RDX, (c) CRCC 100  $\mu\text{m}$ , (d) CRCC 20  $\mu\text{m}$ .

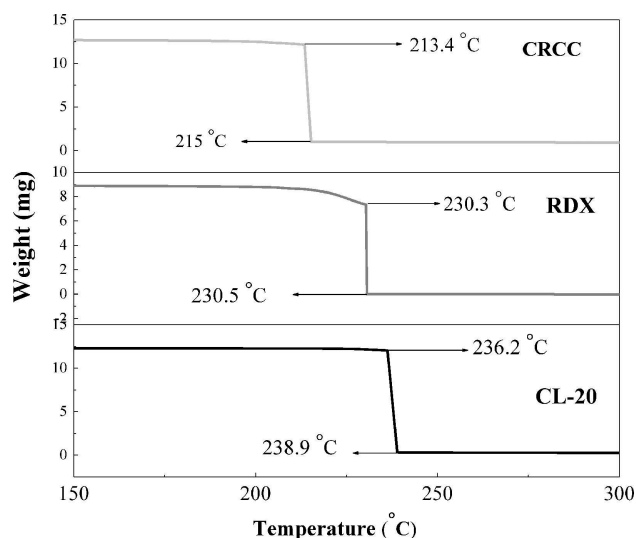


Figure 9. Comparison between TGA profiles of  $\epsilon$ -CL-20, RDX and CRCC

first small endothermic peak at 186.8 °C may be the morphology changes takes place [45]. The next two endothermic peaks at 196.4 °C and 203.7 °C represent the phase transition of  $\epsilon$ -CL-20 and melting point and of CRCC respectively. The entire endothermic range of CRCC lies between the melting point of pure  $\epsilon$ -CL-20 and RDX individually. A sharp single exothermic peak at 215.4 °C represents the single decomposition temperature of cocrystal. The decomposition temperature of cocrystal is low (215 °C) when compared to that of individual sub crystals ( $T_d\epsilon$ -CL-20 = 240 °C;  $T_d$ RDX = 230 °C). This change suggests the formation of cocrystal.

Lead blocks charged with  $\epsilon$ -CL-20 and RDX show an average expansion volume of 975  $\text{cm}^3$  and 615  $\text{cm}^3$  per 10 g respectively, whereas the CRCC shows an average ex-

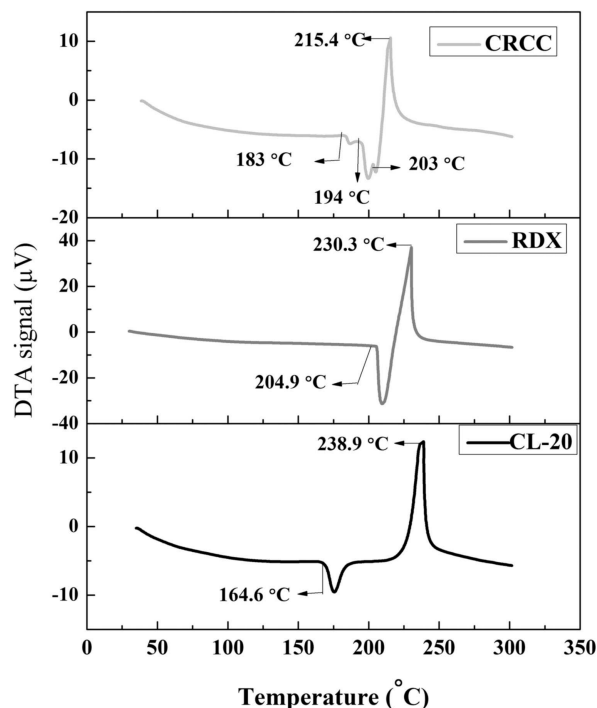


Figure 10. Comparison between DTA profiles of  $\epsilon$ -CL-20, RDX and CRCC

Table 4. Trauzl lead block test results of CRCC,  $\epsilon$ -CL-20 and RDX.

S. No	Name of the sample	Volume increased in $\text{cm}^3$	Average volume in $\text{cm}^3$	Average volume increased /10 g
1	Commercial RDX	18.5	18.45	615
2	$\epsilon$ -CL-20	18.4	29.25	975
3	CRCC	29.2	29.40	980

pansion volume of 980  $\text{cm}^3$  per 10 g. The results obtained indicate that the cocrystal has more energy on comparison to  $\epsilon$ -CL-20 and the higher energy is obtained from breaking of the hydrogen bonds within the CRCC. The results are summarized in Table 4.

9  $\pm$  2% of Steric acid coated aluminium, 0.2  $\pm$  0.1% graphite and  $\sim$ 26  $\pm$  3 mg of test sample ( $\epsilon$ -CL-20, RDX and CRCC) were mixed thoroughly to facilitate the flowability. Uniform particle sizes ( $> 100 \mu\text{m}$ ) were maintained throughout the experiment. Three different batches of test samples were tested, and the highest values of shock tube detonation velocities measured are tabulated in Table 5. The average shock tube detonation velocity of 1864 m/s is recorded for CRCC which is still higher than that of  $\epsilon$ -CL-20 (1614 m/s).

BE obtained using M06-2X and  $\omega$ B97X-D functionals for the 13 conformers are given in the Table 6. All the con-

**Table 5.** Detonation velocities of shock tubes fabricated employing  $\epsilon$ -CL-20, RDX and CRCC.

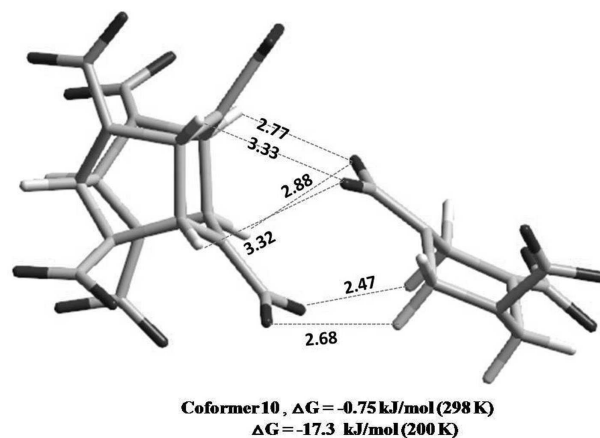
S. No	Identification	Detonation velocity (meter/sec)	Bulk Density (g/cc)
1.	ST <sub>CL-20</sub>	1639	0.98
2.	ST <sub>CL-20</sub>	1623	0.96
3.	ST <sub>CL-20</sub>	1582	0.95
	<b>Average</b>	<b>1614</b>	<b>0.97</b>
4.	ST <sub>RDX</sub>	1552	0.78
5.	ST <sub>RDX</sub>	1524	0.79
6.	ST <sub>RDX</sub>	1506	0.79
	<b>Average</b>	<b>1527</b>	<b>0.79</b>
7.	ST <sub>CRCC</sub>	1953	0.71
8.	ST <sub>CRCC</sub>	1865	0.71
9.	ST <sub>CRCC</sub>	1718	0.71
	<b>Average</b>	<b>1864</b>	<b>0.71</b>

**Table 6.** Calculated binding energy  $\Delta E$ , changes in enthalpy ( $\Delta H$ ), free energy ( $\Delta G$ ) and entropy ( $\Delta S$ ) of various conformers 1–13 of co-crystal RDX/CL-20 obtained at  $\omega$ B97XD/6-31G(D,P) at 298 K. Values in brackets are from M06-2X/6-31G(D,P) at 298 K.

Conformer	$\Delta E$ kJ/mol	$\Delta H$ kJ/mol	$\Delta G$ kJ/mol	$\Delta S$ J/mol-K
1	−63.30 (−80.83)	−56.32 (−75.14)	2.18 (−13.18)	−196.10 (−207.82)
2	−61.80 (−53.43)	−52.47 (−50.38)	4.73 (−4.48)	−191.84 (−172.88)
3	−36.69 (−55.94)	−29.75 (−50.38)	29.46 (−12.68)	−198.57 (−211.46)
4	−18.37 (−21.21)	−12.97 (−15.69)	23.68 (−28.58)	−122.97 (−148.45)
5	−45.10 (−48.53)	−35.31 (−42.09)	11.42 (−6.82)	−156.77 (−164.14)
6	−59.33 (−77.15)	−53.30 (−71.63)	2.01 (−7.91)	−185.43 (−213.72)
7	−52.97 (−61.34)	−48.41 (−56.40)	7.53 (−2.30)	−187.53 (−196.82)
8	−41.21 (−45.56)	−32.97 (−38.79)	8.03 (−9.41)	−137.40 (−161.67)
9	−63.51 (−78.16)	−54.98 (−71.42)	0.92 (−13.26)	−187.49 (−195.10)
10	−57.61 (−69.62)	−51.21 (−63.64)	−0.75 (−10.33)	−169.20 (−178.78)
10*	−57.62 (−69.53)	−52.77 (−65.20)	−17.63 (−28.19)	−175.70 (−185.09)
11	−25.56 (−29.04)	−19.25 (−23.35)	23.56 (−24.98)	−143.64 (−161.96)
12	−43.68 (−46.69)	−35.73 (−40.00)	13.05 (−14.64)	−163.59 (−183.18)
13	−51.84 (−50.00)	−48.49 (−43.93)	10.13 (−9.58)	−196.61 (−179.49)

\* Values are at 200 K temperature.

formers are showing high binding energies which indicate that there are large intermolecular interactions in the RDX/CL-20 CRCC. Among all Conformer 1 and Conformer 9 are showing almost equal high BE from both the functionals.

**Figure 11.** Optimized geometries of molecules RDX, CL-20 and conformer 10 at  $\omega$ B97X-D. Hydrogen bonding (O–H) distance in conformer 10 are shown in units of Å.

Changes in entropies ( $\Delta S$ ), enthalpy ( $\Delta H$ ) and Gibbs free energy ( $\Delta G$ ) at 298 K are estimated and given in Table 6. Obtained  $\Delta H$  values for all the conformers are negative indicate the exothermic nature of the formation of cocrystal from the isolated molecules. Among all conformers  $\Delta H$  values are found to be largest for conformer 1 that is  $-56.32$  and  $-75.14$  kJ/mol using  $\omega$ B97X-D and M06-2X respectively. Among the conformation studied, largest  $\Delta G$  values are obtained for Conformer 10 ( $-0.75$  kJ/mol) at 298 K and at a lower temperature (200 K) the  $\Delta G$  is  $-17.63$  kJ/mol for the formation of Conformer 10 as shown in the same table. It is clear that the lower temperatures facilitate the formation of the cocrystal. Hydrogen bonding between O and H (O–H) distance in Conformer 10 are shown in Figure 11.

## 5 Conclusion

From the present investigation and the results obtained, it is envisaged that the formation of EECC with  $\epsilon$ -CL-20 and RDX in the ration of 1:1 takes place with 100 times the weight tried earlier [4] and is confirmed on the basis of spectral and other analytical techniques. The phase change from  $\epsilon \rightarrow \alpha$  is also observed during the formation of EECC and it is supported by the XRD and FTIR results. The EECC thus formed from the desired solvent possesses the required parameters of moderate thermal stability so as to be used as a potential candidate for Solid Rocket Propellant (SRP). The applicability of CRCC in shock tubes to initiate detonators is claimed herewith as its applicability is cost effective than CL-20. The theoretical investigation revealed that entropy changes play a predominant role in the formation and stabilization of a particular conformer, and it is predicted from the theoretical investigation that the formation of CRCC is facilitated at a lower temperature. The

mechanical sensitivity of CRCC and the parameters influencing the reduction in mechanical sensitivity of CL-20 shall be discussed later.

## Acknowledgement

The author, JVV is thankful to Premier Explosives Limited, Hyderabad for the financial support (H/Ac.No.4254). the authors KBP and BS thank the Director, CSIR-IICT(IICT/Pubs.2018/240), for the constant encouragement in this work. Funds from CSIR(CSC-0107-IN-SPIRE) is gratefully acknowledged. This work is carried out under the Gulbarga University-CSIR-IICT MoU exchange program.

## References

- [1] D. Trache, T. M. Klapotke, L. Maiz, M. And-Elghany, L. T. DeLuca, Recent advances in new oxidizers for solid rocket propulsion, *Green Chem.* **2017**, *19*, 4711–4736.
- [2] J. Venkata Viswanath, K. J. Venugopal, N. V. Srinivasa Rao, A. Venkataraman, An overview on importance, synthetic strategies and studies of 2,4,6,8,10,12-hexanitro-2,4,6,8,10,12-hexaazaisowurtzitane (HNIW), *Defence Technology.* **2016**, *12*, 401–418.
- [3] J. Venkata Viswanath, P. Vijayadarshan, T. Mohan, N. V. Srinivasa Rao, Amarnath Gupta, A. Venkataraman, Copper chromite as ballistic modifier in a typical solid rocket propellant composition: A novel synthetic route involved, *J. Energ. Mater.* **2017**, *36*, 69–81.
- [4] H. Gao, W. Jiang, J. Liu, G. Hao, L. Xiao, X. Ke, T. Chen, Synthesis and characterization of new co-crystal explosive with high energy and good sensitivity, *J. Energ. Mater.* **2017**, *35*, 490–498.
- [5] X. Wei, A. Zhang, Y. Ma, X. Xue, J. Zhou, Y. Zhu, C. Zhang, Towards low-sensitive and high-energetic cocrystal III: thermodynamics of energetic-energetic cocrystal formation, *CrystEngComm.* **2015**, *17*, 9037–9047.
- [6] Z. Yang, H. Li, X. Zhou, C. Zhang, H. Huang, J. Li, F. Nie, Characterization and properties of a novel energetic-energetic cocrystal explosive exposed of HNIW and BTF, *Cryst. Growth Des.* **2012**, *12*, 5155–5158.
- [7] G.-Y. Hang, W.-L. Yu, T. Wang, J.-T. Wang, Z. Li, Theoretical insights into effects of molar ratios on stabilities, mechanical properties and detonation performance of CL-20/RDX cocrystal explosives by molecular dynamics simulation, *J. Mol. Struct.* **2017**, *1141*, 577–583.
- [8] G. F. Brent, M. D. Harding, Shock tube initiator US Patent 5,243,913, Imperial Chemical Industries PLC, London, UK, **1993**.
- [9] N. Qiao, M. Li, W. Schlindwein, N. Malek, A. Davies, G. Trappitt, Pharmaceutical cocrystals: an overview, *Int. J. Pharm.* **2011**, *419*, 1–11.
- [10] H. Gao, P. Du, X. Ke, J. Liu, G. Hao, T. Chen, W. Jiang, A novel method to prepare Nano-sized CL-20/NQ co-crystal: Vacuum freeze drying, *Propellants Explos. Pyrotech.* **2017**, *42*, 889–895.
- [11] C. Zhang, X. Xue, Y. Cao, Y. Zhou, H. Li, J. Zhou, T. Gao, Intermolecular friction symbol derived from crystal information, *CrystEngComm.* **2013**, *15*, 6837–6844.
- [12] N. Sen, A 1:1 Energetic co-crystal formed between trinitrotoluene and 2,3-diaminotoluene, *Macedonian Journal of Chemistry and Chemical Engineering.* **2018**, *37*, 61–69.
- [13] M. Frances Foltz, C. L. Coon, Frank Garcia, A. L. Nichols III, The thermal stability of the polymorphs of hexanitrohexaazaisowurtzitane, part-II, *Propellants Explos. Pyrotech.* **1994**, *19*, 19–25.
- [14] D. Mark Hoffman, Voids and density distribution in 2,4,6,8,10,12-hexanitro-2,4,6,8,10,12-hexaazaisowurtzitane (CL-20) prepared under various conditions, *Propellants Explos. Pyrotech.* **2003**, *28*, 194–200.
- [15] C. Zhang, X. Xue, Y. Cao, J. Zhou, A. Zhang, H. Li, Y. Zhou, R. Xu, T. Gao, Towards Low-sensitive and high-energetic co-crystal II: Structural, electronic and energetic features of CL-20 polymorphs and the observed CL-20-based energetic-energetic co-crystal, *CrystEngComm.* **2014**, *16*, 5905–5916.
- [16] L. Turker, S. Varis, Structurally modified RDX—A DFT study, *Defence Technology.* **2017**, *13*, 385–391.
- [17] C. Guo, H. Zhang, X. Wang, J. Xu, Y. Liu, X. Liu, H. Huang, J. Sun, Crystal structure and explosive performance of a new CL-20/caprolactam cocrystal, *J. Mol. Struct.* **2013**, *1048*, 267–273.
- [18] A. Matzger, O. Bolton, *Crystalline explosive material*, US Patent 9,096,530 B2, Ann Arbor, MI, US, **2015**.
- [19] M. Ghosh, A. K. Sikder, S. Banerjee, G. G. Rajesh, Studies of CL-20/HMX (2:1) cocrystal: A new preparation method and structural and thermokinetic analysis, *Cryst. Growth Des.* **2018**, *18*, 3781–3793.
- [20] Z. Yang, Q. Zeng, X. Zhou, Q. Zhang, F. Nie, H. Huang, H. Li, Cocrystal explosive hydrate of powerful explosive, HNIW, with enhanced safety, *RSC Adv.* **2014**, *4*, 65121–65126.
- [21] X. Wei, Y. Ma, X. Long, C. Zhang, A strategy developed from the observed energetic-energetic cocrystals of BTF: cocrystallizing and stabilizing energetic hydrogen-free molecules with hydrogenous energetic conformer molecules, *CrystEngComm.* **2015**, *17*, 7150–7159.
- [22] S. Zeman, M. Jungova, Sensitivity and performance of energetic materials, *Propellants Explos. Pyrotech.* **2016**, *41*, 426–451.
- [23] D. Spitzer, B. Risse, F. Schnell, V. Pichot, M. Klumunzer, M. R. Schaefer, Continuous engineering of nano-cocrystals for medical and energetic applications, *Sci. Rep.* **2014**, *4*, Article 6575, 1–6.
- [24] B. Gao, D. Wang, J. Zhang, Y. Hu, J. Shen, J. Wang, B. Huang, Z. Qiao, H. Huang, F. Nie, G. Yang, Facile Continuous and large-scale synthesis of CL-20/HMX nano co-crystals with high performance by ultrasonic spray assisted electrostatic adsorption method, *J. Mater. Chem. A.* **2014**, *2*, 19969–19974.
- [25] H. Qiu, R. B. Patel, R. S. Damavarapu, V. Stepanov, Nanoscale 2CL-20: HMX high explosive cocrystal synthesized by bead milling, *CrystEngComm.* **2015**, *17*, 4080–4083.
- [26] C. An, H. Li, B. Ye, J. Wang, Nano CL-20/HMX cocrystal explosive for significantly reduced mechanical sensitivity, *J. Nanomater.* **2017**, *2017*, Article ID 3791320, 7 pages, <http://doi.org/10.1155/2017/3791320>.
- [27] H. Xu, X. Duan, H. Li, C. Pei, A novel high-energetic and good-sensitive cocrystal composed of CL-20 and TATB by a rapid solvent/non-solvent method, *RSC Adv.* **2015**, *5*, 95764–95770.
- [28] Methods of test for commercial blasting explosives and accessories, Indian standards institution, New Delhi, India. IS: 6609 (PartII/Sec I)-**1973**.
- [29] S. Plimpton, Fast Parallel Algorithms for Short-Range Molecular Dynamics, *J. Comp. Physiol.* **1995**, *117*, 1–19.
- [30] J. Wang, R. M. Wolf, J. W. Caldwell, P. A. Kollman, D. A. Case, Development and Testing of a General Amber Force Field, *J. Comput. Chem.* **2004**, *25*, 1157–1174.
- [31] A. I. Jewett, Z. Zhuang, J. E. Shea, Moltemplate a coarse-grained model assembly tool, *Biophys. J.* **2013**, *104*, 169a.
- [32] C. I. Bayly, P. Cieplak, W. Cornell, P. A. Kollman, A Well Behaved Electrostatic Potential Based Method Using Charge Restraints

- for Deriving Atomic Charges: The Resp Model, *J. Phys. Chem.* **1993**, *97*, 10269–10280.
- [33] W. D. Cornell, P. Cieplak, C. I. Bayly, I. R. Gould, K. M. Merz, D. M. Ferguson, D. C. Spellmeyer, T. Fox, J. W. Caldwell, P. A. Kollman, A Second Generation Force Field for the Simulation of Proteins, Nucleic Acids, and Organic Molecules, *J. Am. Chem. Soc.* **1995**, *117*, 5179–5197.
- [34] R. W. Hockney, J. W. Eastwood, Computer simulation using particles, Boca Raton: CRC Press; **1988**.
- [35] J.-D. Chai, M. Head-Gordon, Long-range corrected hybrid density functionals with damped atom-atom dispersion corrections, *Phys. Chem. Chem. Phys.* **2008**, *10*, 6615–6620.
- [36] Y. Zhao, D. G. Truhlar, The M06 suite of density functional for main group thermochemistry, thermochemical kinetics, non-covalent interactions, excited states, and transition elements: two new functionals and systematic testing of four M06-class functional and 12 other functional, *Theor. Chem. Acc.* **2008**, *120*, 215–241.
- [37] Y. Zhao, D. G. Truhlar, Density functionals with broad applicability in chemistry, *Acc. Chem. Res.* **2008**, *41*, 157–167.
- [38] Gaussian 09, Revision B.01, M. J. Frisch, G. W. Trucks, H. B. Schlegel, G. E. Scuseria, M. A. Robb, J. R. Cheeseman, G. Scalmani, V. Barone, B. Mennucci, G. A. Petersson, H. Nakatsuji, M. Caricato, X. Li, H. P. Ratchian, A. F. Izmaylov, J. Bloino, G. Zheng, J. L. Sonnenberg, M. Hada, M. Ehara, K. Toyota, R. Fukuda, J. Hasegawa, M. Ishida, T. Nakajima, Y. Honda, O. Kitao, H. Nakai, T. Vreven, J. A. Montgomery, Jr., J. E. Peralta, F. Ogliaro, M. Bearpark, J. J. Heyd, E. Brothers, K. N. Kudin, V. N. Staroverov, T. Keith, R. Kobayashi, J. Normand, K. Raghavachari, A. Rendell, J. C. Burant, S. S. Iyengar, J. Tomasi, M. Cossi, N. Rega, J. M. Millam, M. Klene, J. E. Knox, J. B. Cross, V. Bakken, C. Adamo, J. Jaramillo, R. Gomperts, R. E. Stratmann, O. Yazyev, A. J. Austin, R. Cammi, C. Pomelli, J. W. Ochterski, R. L. Martin, K. Morokuma, V. G. Zakrzewski, G. A. Voth, P. Salvador, J. J. Dannenberg, S. Dapprich, A. D. Daniels, O. Farkas, J. B. Foresman, J. V. Ortiz, J. Cioslowski, D. J. Fox, Gaussian, Inc., Wallingford CT, **2010**.
- [39] B. K. Mishra, S. Karthikeyan, V. Ramanathan, Tuning the C–H... $\pi$  interaction by different substitutions in benzene-acetylene complexes, *J. Chem. Theory Comput.* **2012**, *8*, 1935–1942.
- [40] H. Chen, S. Chen, L. Li, S. Jin, Quantitative determination of  $\epsilon$ -phase in polymorphic HNIW using X-ray diffraction pattern, *Propellants Explos. Pyrotech.* **2008**, *33*, 467–471.
- [41] M. J. Herrmann, Characterization of the microstructure of the energetic materials, Technical report submitted to European office of aerospace research and development, London, England, Fraunhofer Institut für Chemische Technologie, Germany, **2003**.
- [42] M. Ghosh, V. Venkatesan, S. Mandave, S. Banerjee, N. Sikder, A. K. Sikder, Bikash Bhattacharya, Probing crystal growth of  $\epsilon$ - and  $\alpha$ -CL-20 polymorphs via metastable phase transition using microscopy and vibrational spectroscopy, *Cryst. Growth Des.* **2014**, *14*, 5053–5063.
- [43] E. von Holtz, D. Ornellas, M. Frances Foltz, J. E. Clarkson, The solubility of  $\epsilon$ -CL-20 in selected materials, *Propellants Explos. Pyrotech.* **1994**, *19*, 206–212.
- [44] H. Dou, K.-H. Kim, B.-C. Lee, J. Choe, H.-S. Kim, S. Lee, Preparation and characterization of cyclo-1,3,5-trimethylene-2,4,6-trinitramine (RDX) powder: Comparison of microscopy, dynamic light scattering and field-flow fractionation for size characterization, *Powder Technol.* **2013**, *235*, 814–822.
- [45] C. Guo, D. Wang, B. Gao, J. Wang, B. Luo, G. Yang, F. Nie, Solid-solid phase transition study of  $\epsilon$ -CL-20/binders composites, *RSC Adv.* **2016**, *6*, 859–865.

Manuscript received: April 17, 2019

Revised manuscript received: June 27, 2019

Version of record online: September 18, 2019